



Two-dimensional analysis of PEM fuel cells

B. HUM and XIANGUO LI*

Department of Mechanical Engineering, University of Waterloo, Waterloo, Ontario, Canada N2L 3G1

*(*author for correspondence, fax: +1-519-888-6197, e-mail: xgli@uwaterloo.ca)*

Received 12 March 2002; accepted in revised form 26 August 2003

Key words: current distribution, electrochemical reaction, fuel cell, mass transfer, numerical simulation, PEM

Abstract

This study reports a two-dimensional numerical simulation of a steady, isothermal, fully humidified polymer electrolyte membrane (PEM) fuel cell, with particular attention to phenomena occurring in the catalyst layers. Conservation equations are developed for reactant species, electrons and protons, and the rate of electrochemical reactions is determined from the Butler–Volmer equation. Finite volume method is used along with the alternating direction implicit algorithm and tridiagonal solver. The results show that the cathode catalyst layer exhibits more pronounced changes in potential, reaction rate and current density generation than the anode catalyst layer counterparts, due to the large cathode activation overpotential and the relatively low diffusion coefficient of oxygen. It is shown that the catalyst layers are two-dimensional in nature, particularly in areas of low reactant concentrations. The two-dimensional distribution of the reactant concentration, current density distribution, and overpotential is determined, which suggests that multi-dimensional simulation is necessary to understand the transport and reaction processes occurring in a PEM fuel cell.

1. Introduction

Polymer electrolyte membrane (PEM) fuel cells have increasingly become promising for zero-emission vehicle and on-site cogeneration applications due to their fast startup, high energy efficiency and high power density. Over the last decade, significant technical progress has been made towards commercial applications. Despite rapid progress being made, substantial cost reduction and cell performance improvement are required before PEM fuel cell can reach widespread commercial use [1]. It has been recognized [2] that the most promising direction for performance improvement is based on the minimization of all transport resistances.

There have been many analyses and modeling efforts for transport phenomena in PEM fuel cells, most of which can be categorized into three groups: the first is the empirical correlations for the performance of a single cell or a stack of multiple cells in terms of the cell/stack voltage–current relations [3–6], this approach has a limited applicability due to the lack of fundamental understanding of the phenomena involved and the lack of universality of the empirical constants under different design and operating conditions. The second is the detailed CFD-based simulation of reactant gas flows, but electrochemical reactions in the catalyst layers is either neglected completely or assumed to have infinitely large reaction rate [7–11], hence the entire catalyst layers, the heart and soul of fuel cells, are simplified into

an infinitesimally thin mathematical surface – an unrealistic and simplistic approach for the analysis of the fuel cell itself, even though complex fluid flow and transport phenomena in the flow channels are modeled through the numerical simulation based on computational fluid dynamics. The third group takes into account both the electrochemical reactions in the catalyst layers, and the physical transport of reactant gas flows, product and process water, heat and the charged species in the individual cells and stacks, hence it is the most comprehensive approach in the modeling and investigation of transport phenomena and their impact on PEM fuel cell performance. This approach has been adopted by our group [12–17], among others [18], including the optimal catalyst layer composition, cell performance, liquid water flooding, carbon monoxide poisoning of the anode catalyst, reactant humidification and membrane hydration, operation with reformed fuel and pressurization, as well as stack design with various stack configurations and reactant flow manifold layouts. Because of the complexities involved in this third approach, most of the studies have adopted one-dimensional formulation, which is reasonable for a small single cell for laboratory tests. For practical PEM fuel cells of large cell sizes, multi-dimensional formulation is necessary in order to account for local phenomena such as local hot spot formation. Experimental techniques have also been developed to measure the two-dimensional distributions

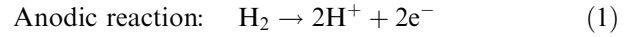
of current [19] in order to quantify the multi-dimensional effect of the transport phenomena on the cell performance.

In this study a two-dimensional simulation is reported for a steady isothermal and fully hydrated PEM fuel cell. The governing equations are formulated based on the conservation principle for the reactant species (hydrogen and oxygen), electrons and protons. The transport of the electrons in the conducting solids in the electrode-backing layers and the catalyst layers, and the protons in the membrane region and through the membrane electrolyte in the catalyst layers is expressed in terms of the electronic and protonic currents, respectively, with different conductivities for the various regions involved. Both the mass transfer and electrochemical reactions are accounted for in the catalyst layers, and the rate of electrochemical reactions is determined by the Butler–Volmer equation. The present study represents our efforts in the multi-dimensional analysis of the transport and electrochemical phenomena occurring inside a PEM fuel cell, and such an approach can be combined with the detailed CFD-based simulation of the fluid flow and transport processes in the reactant flow channels to form a comprehensive multi-dimensional simulation of the practical PEM fuel cells.

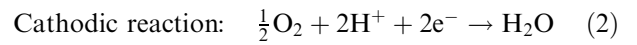
2. Formulation

Figure 1 shows a schematic of PEM fuel cell structure. Typically humidified hydrogen gas is provided through

the anode flow channel to the anode electrode-backing layer, through which the hydrogen fuel diffuses to the anode catalyst layer for the oxidation reaction:



The protons produced migrate through the membrane electrolyte to reach the cathode catalyst layer, and the electrons transport through the external circuit doing work on the load, which constitutes the electric power output, before arriving at the cathode. At the cathode side, humidified oxygen gas is supplied via the cathode flow channel to the cathode electrode-backing layer and diffuses to the cathode catalyst layer for the reduction reaction:



Therefore, there are a total of five regions to be analyzed, including the electrode-backing layers and the catalyst layers in the anode and cathode, respectively, and the membrane electrolyte region, as shown schematically in Figure 1.

As a first attempt, the above multi-dimensional transport phenomena are assumed to be steady, isothermal, and two-dimensional with constant thermo-physical properties. The reactant gas mixture is fully saturated by water vapor and follows ideal gas behavior. The porous electrode backing and catalyst layers are assumed macro-homogeneous, and diffusion process in the porous structure is predominant with negligible convection effect. The membrane electrolyte is assumed

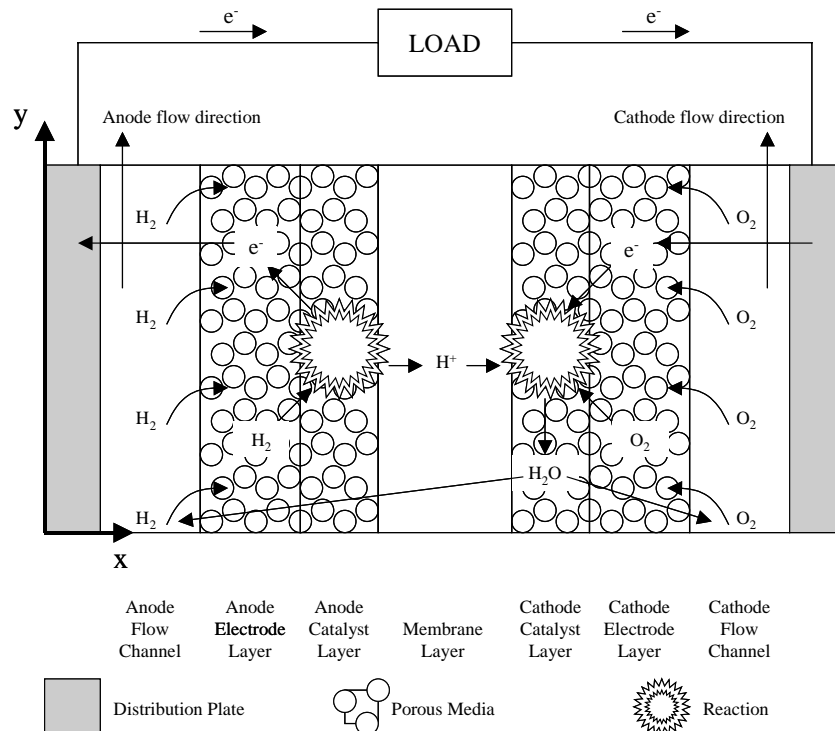


Fig. 1. Schematic of transport and electrochemical processes in PEM fuel cells.

fully hydrated to simplify the proton transfer. Then, the equations for the conservation of reactant species (namely, hydrogen and oxygen molecules), electrons and protons in the electrode-backing layers and the catalyst layers become

$$\text{Reactant: } \nabla \cdot (D_i^{\text{eff}} \nabla c_i) - \frac{s_i}{nF} R_i = 0 \quad (3)$$

$$\text{Electron: } \nabla \cdot (\sigma_s^{\text{eff}} \nabla V_s) - R_i = 0 \quad (4)$$

$$\text{Proton: } \nabla \cdot (\sigma_m^{\text{eff}} \nabla V_m) + R_i = 0 \quad (5)$$

for both the anode and cathode electrodes, where the subscript ‘ i ’ represents the reactant species, and $s_i = -2$ for H_2 and $-1/2$ for O_2 , respectively; σ_s^{eff} (S m^{-1}) and σ_m^{eff} (S m^{-1}) are the effective conductivity of electron through the solid electrode structure and proton through the membrane region, respectively, and they are determined with Bruggeman’s correction of the bulk conductivity values [13]; D_i^{eff} ($\text{m}^2 \text{s}^{-1}$) is the effective diffusion coefficient of the reactant (H_2 in the anode and O_2 in the cathode), determined with Bruggeman’s correction due to the porous nature of the electrode structure and Henry’s law of solubility if the structure is flooded by liquid water [14]; c (mol m^{-3}) is the reactant concentration; V_s (V) and V_m (V) are the electrical potential in the solid electrode and membrane electrolyte, respectively; n is the number of electrons transferred in the half-cell reaction shown in Equations 1 and 2, hence $n=2$; F is the Faraday constant; and R (A m^{-3}) is the rate of electrochemical reaction shown in Equations 1 and 2, expressed in terms of the volumetric rate of current generation. Using the Butler–Volmer equation for the heterogeneous electrochemical reaction, the reaction rate becomes

$$R_i = aj_{0,\text{ref}} \left(\frac{C_i}{C_{i,\text{ref}}} \right)^{\gamma_i} \left\{ \exp \left[\frac{\alpha_a n F}{\mathcal{R} T} (V_s - V_m) \right] - \exp \left[-\frac{\alpha_c n F}{\mathcal{R} T} (V_s - V_m) \right] \right\} \quad (6)$$

where a ($\text{m}^2 \text{m}^{-3}$) is the density of the catalyzed active area in the catalyst layer; $j_{0,\text{ref}}$ (A m^{-2}) is the exchange current density at the reference reactant concentration of $C_{i,\text{ref}}$ (mol m^{-3}), γ_i is the overall reaction order with respect to the reactant species i , α_a and α_c are the apparent transfer coefficient for the anodic and cathodic reactions of the two half-cell reactions given in Equations 1 and 2; \mathcal{R} ($\text{J mol}^{-1} \text{K}^{-1}$) is the universal gas constant; and T is the temperature in Kelvin. Clearly, the transport process of the reactant species i is closely related to the transport of the electrons and protons through the above rate of electrochemical reactions.

It should be pointed out that the catalyzed heterogeneous reaction occurs in the anode and cathode catalyst layers only, therefore, $R_i=0$ for the electrode-backing

layer and the membrane electrolyte layer, where pure membrane exists so that the proton migration is governed by the following equation with the membrane bulk conductivity σ_m (S m^{-1})

$$\nabla \cdot (\sigma_m \nabla V_m) = 0 \quad (7)$$

The boundary conditions that the above governing equations should satisfy are:

(i) at the electrode surface facing the flow channel:

$$c_i = c_{i,0} (\text{mol m}^{-3}); V_s = V_{s,a} \text{ (V) for the anode; and } V_s = V_{s,c} \text{ (V) for the cathode} \quad (8)$$

(ii) at the top and bottom surfaces, no leakage for the species, electron and proton fluxes:

$$\frac{\partial}{\partial y} \{c_i, V_s, V_m\} = 0 \quad (9)$$

Further, the following internal boundary conditions must be satisfied as well:

(iii) at the interface between the electrode-backing layer and the catalyst layer:

$$\frac{\partial V_m}{\partial x} = 0 \quad (10)$$

(iv) at the interface between the catalyst layer and the membrane electrolyte region:

$$\frac{\partial V_s}{\partial x} = 0 \quad (11)$$

Once the governing equations are solved subject to the above internal and external boundary conditions, the current density distribution in the electrode-backing layer and membrane electrolyte region can be obtained, respectively, by

$$\vec{j}_s = -\sigma_s^{\text{eff}} \nabla V_s \quad (12)$$

$$\vec{j}_m = -\sigma_m^{\text{eff}} \nabla V_m \text{ or } \vec{j}_m = -\sigma_m \nabla V_m \quad (13)$$

where \vec{j}_s (A m^{-2}) and \vec{j}_m (A m^{-2}) represents the electronic and protonic current density, respectively. Notice that the current density is a vector quantity, and only the x -component (i.e., normal to the electrode surface) is useful, contributing to the power output from the cell; while the y -component only contributes to the degradation of useful energy, hence, should be minimized or avoided if possible through appropriate cell structure design.

3. Numerical technique

The governing Equations 3–5 and 7 are of Poisson and Laplace type, and can be written in the following generic form:

$$\nabla \cdot (\Gamma \nabla \phi) + S_P = 0 \quad (14)$$

where Γ represents the diffusion coefficient; ϕ is the generic variable representing the reactant concentration c_i , and electrical potential in the solid and membrane, V_s and V_m , respectively; S_P is the generic source term. Then Equation 14 is discretized by the finite volume technique, and the discretized equations are solved by the alternating direct implicit method. Non-uniform grid is used with local clustering as described in [20].

The reactant concentration, $c_{i,0}$, in the boundary condition, Equation 8, is calculated based on the cell operating temperature and pressure for the fully saturated reactant mixture, and the electrical potential at the anode and the cathode, $V_{s,a}$ and $V_{s,c}$, are specified. The voltage drop across the cell represents the voltage loss or the cell overpotentials, η_{cell} (V),

$$\eta_{\text{cell}} = V_{s,a} - V_{s,c} \quad (15)$$

For convenience, $V_{s,c}$ is set to 0. Then the actual cell potential difference V_{cell} (V) is obtained as

$$V_{\text{cell}} = V_{\text{rev}} - \eta_{\text{cell}} \quad (16)$$

where V_{rev} (V) is the reversible cell potential, determined similarly to [13, 14]. Further details of the model formulation and the numerical techniques employed in the present study are available elsewhere [21].

4. Results and discussion

For all the results presented in this study, the fuel cell is assumed to consist of 200 μm thick electrode-backing layer, 10 μm thick catalyst layer and 230 μm thick membrane region of Nafion 117. The cell height is taken as 10 mm from symmetry consideration of the practical cells. A porosity of 40% is used for both the electrode-backing and the catalyst layers. Fully humidified H_2 and O_2 are considered as the anode and cathode reactant,

respectively. The cell operating temperature is 353 K (or 80 °C), the anode and cathode inlet gas mixture pressure is 3 and 5 bar, respectively. This yields a reversible cell voltage of $V_{\text{rev}} = 1.2058$ V. The physical and kinetic data used in the model calculations are given in Table 1, these data are compiled based on the experimental data available in the literature and used in our previous studies [13–15].

One-dimensional results are obtained first for its simplicity in the model calculation and for its clarity in the result presentation. These results correspond to the fuel and oxidant utilization of 0%, equivalent to very high stoichiometry (or the reactant flow rate) used, thus they are useful for better understanding of the two-dimensional results to be presented later on in this section. Figure 2 shows a typical potential distribution across the cell for the cell overpotential of $\eta_{\text{cell}} = V_{s,a} - V_{s,c} = 0.35$ V (or $V_{\text{cell}} = 0.8558$ V); a magnified view for the catalyst layers is shown in Figure 2b. It is seen that the solid potential decreases linearly in the electrode-backing layer due to ohmic loss, then remains almost linear in the anode catalyst layer. However, the membrane phase potential V_m decreases very quickly, almost exponential (Figure 2b) in the anode catalyst layer due to the need of the potential difference between the solid catalyst and the membrane phase to drive up the rate of reaction, although it is a linear drop again in the membrane region due to ohmic resistance to proton transport. It is also shown that for this relatively high cell potential, the largest voltage drop occurs in the membrane region, and the second largest occurs in the cathode catalyst layer (the potential difference between the membrane and the solid phase, or $|V_s - V_m|$), whereas the voltage loss in the anode catalyst layer is negligibly small due to the much fast hydrogen oxidation kinetics. The voltage loss in the electrode backing layer is also seen appreciable for the relative low conductivity of the electrode materials shown in Table 1. It is interesting to notice in Figure 2b that the overpotential in the anode catalyst layer, $\eta_a = V_s - V_m$, decreases first from the interface between the anode electrode-backing and anode catalyst layer, gradually reaches a minimum value in the middle of the anode catalyst layer, and then increases considerably towards the interface between the anode catalyst layer and the membrane electrolyte region – such a behavior may not be apparent from intuition.

Table 1. Physical and kinetic parameter values used in the present study

Parameter	Anode (or H_2)	Cathode (or O_2)
Electrode conductivity, σ_s (S/m^{-1})	114	114
Membrane bulk conductivity, σ_s (S/m^{-1})	15	15
Reference kinetic parameter, $aj_{o,\text{ref}}$ (A/m^{-3})	1.4×10^{11}	10
Reference concentration, c_i (mol m^{-3})	56.4	3.39
Anodic transfer coefficient, α_a	0.5	2.0
Cathodic transfer coefficient, α_c	0.5	2.0
Reaction order, γ_i	0.25	0.5

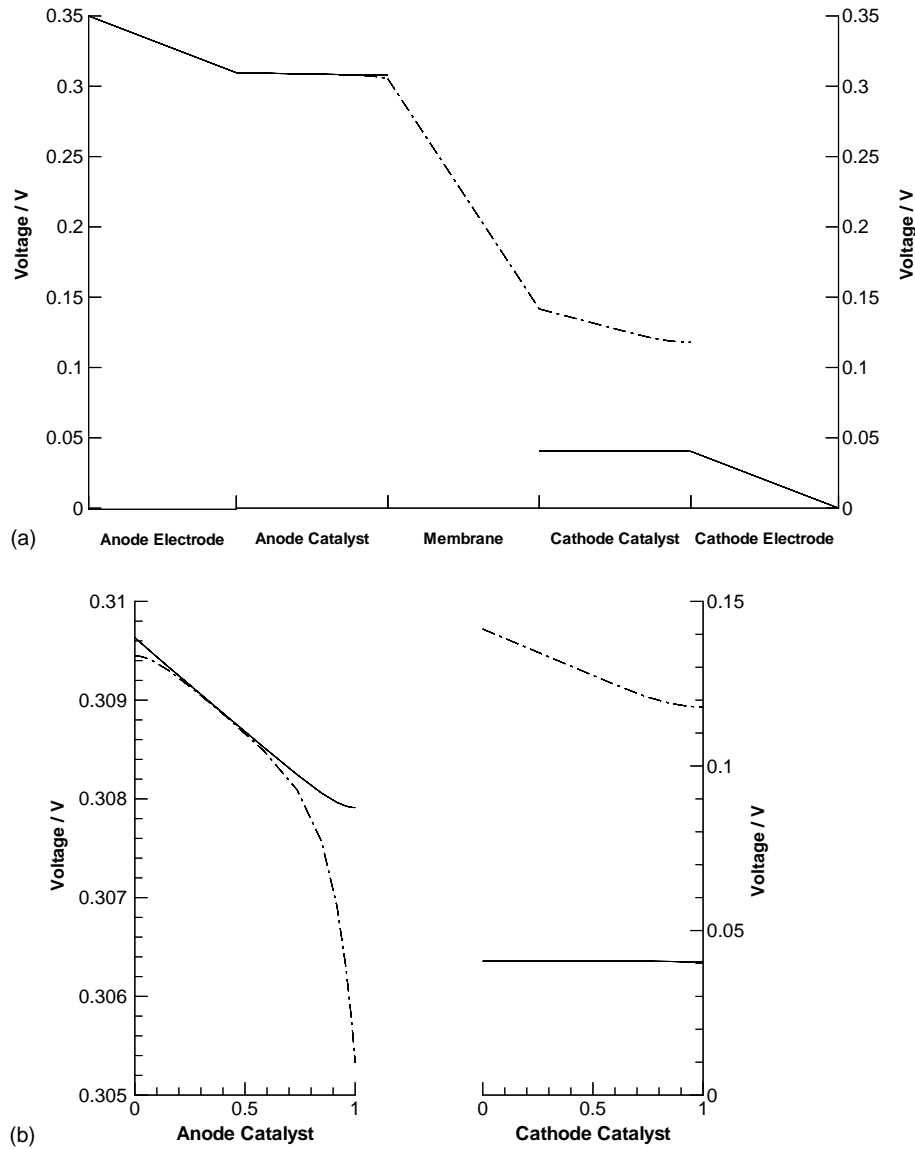


Fig. 2. Potential distribution across the entire cell (a) and the close-up view for the catalyst layer (b) for 1-D simulation at $\eta_{\text{cell}} = 0.35$ V. Solid phase voltage, V_s ; solid line; membrane phase voltage, V_m ; dot-dashed line.

Figure 3 shows the distribution of reactant concentration for hydrogen in the anode and oxygen in the cathode. It is seen that as the rate of reaction is increased, indicated by the cell potential drop η_{cell} increase, the hydrogen and oxygen concentration are lowered in the respective catalyst layer, whose thickness has been magnified in the figure relative to the electrode-backing layer. The concentration distribution is almost linear in the electrode-backing layer, indicating the dominant diffusion process there. It is interesting to point out that at $\eta_{\text{cell}} = 0.35$ V, the oxygen concentration in the cathode catalyst layer is extremely low – almost vanishes, suggesting that the oxygen reduction reaction may occur very close to the interface between the backing and catalyst layer. This is indeed the case, as shown in Figure 4 for the distribution of the protonic and electronic current density in the anode and the cathode catalyst layer. It is evident from the results for

j_m and j_s in the cathode catalyst layer that the rate of oxygen reduction reaction, which is proportional to the rate of proton or electron consumption, is confined to a region close to the catalyst layer interface with the electrode-backing layer. At the higher rate of reaction (i.e., larger values of η_{cell}), the oxygen reduction reaction will become confined to a much narrower region in the catalyst layer, primarily due to the limited rate of oxygen mass transfer dominated by diffusion process. On the other hand, much fast hydrogen mass transfer can supply sufficient hydrogen to the anode catalyst layer to avoid the hydrogen depletion there, therefore, the entire anode catalyst layer is utilized for the hydrogen oxidation reaction, as shown in Figure 4, and much smaller overpotential for the hydrogen oxidation reaction as compared to the oxygen reduction reaction in the cathode catalyst layer, shown in Figure 2b.

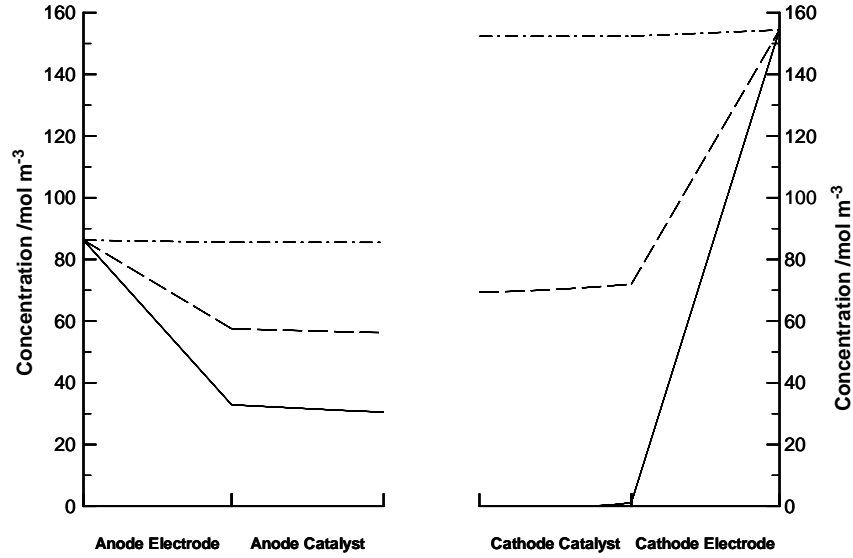


Fig. 3. Reactant concentration distribution for 1-D simulation. Anode for H_2 , cathode for O_2 . $\eta_{\text{cell}} = 0.05$ V: dot-dash line; $\eta_{\text{cell}} = 0.20$ V: dash line; $\eta_{\text{cell}} = 0.35$ V: solid line.

Two-dimensional results are obtained by using finite values for the hydrogen and oxygen utilization; therefore, the reactant concentration will decrease from the flow channel inlet to the outlet, due to the consumption of the reactants by the in-cell electrochemical reactions, producing the two-dimensional phenomena sought in this study. Non-uniform grids are employed in this study with local clustering around the top and bottom surfaces as well as the interfaces between the five layers of the PEM fuel cells, and successive grid refinement study is carried out to ensure the grid-independent results are obtained [21].

Figure 5 shows the distribution of the electrical potential across the cell structure at the cell overpotential of $\eta_{\text{cell}} = 0.26$ V when the fuel and oxidant stream

are in a co-flow arrangement. The utilization for hydrogen is 80% and for oxygen is 50%, corresponding to 80% of the hydrogen consumed from the anode flow channel inlet to the outlet, and 50% reduction of the oxygen concentration in the oxidant stream from the cathode flow channel inlet to the outlet. It is seen that the constant potential surfaces in the electrode-backing layers and the membrane region are almost parallel to the electrode surface, suggesting that 1-D analysis for the potential distribution in these regions may be made, because the electrode surfaces facing the flow channels have been enforced as iso-potential surfaces, i.e., $V_{s,a}$ at the anode electrode/flow channel interface and $V_{s,c}$ at the cathode electrode/flow channel interface are kept constant, respectively, during the model calculation –

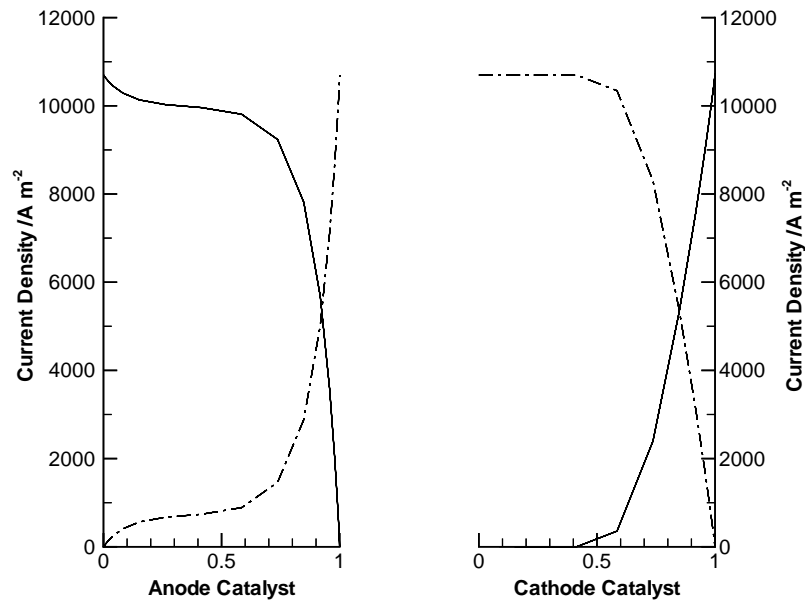


Fig. 4. Current density distribution for 1-D simulation at $\eta_{\text{cell}} = 0.35$ V. protonic current, j_m : dot-dash line; electronic current, j_s : solid line.

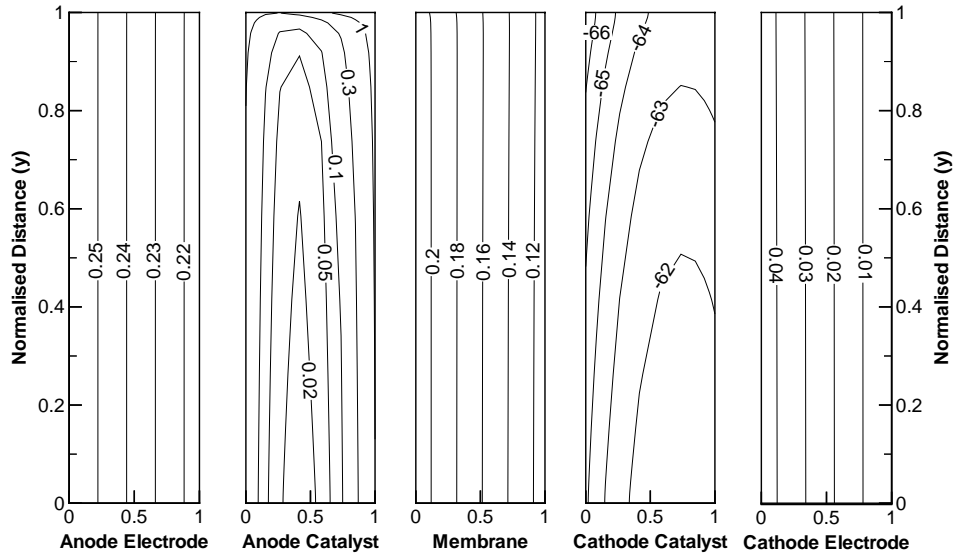


Fig. 5. Electrical potential distribution across the cell for $\eta_{\text{cell}} = 0.26$ V and co-flow of reactant streams. Solid potential, V_s (V), in the electrode-backing layer; V_m (V), in the membrane electrolyte region; and the potential difference, $V_s - V_m$ (mV), in the catalyst layer. The catalyst layer thickness has been magnified significantly for the clarity of presentation.

equivalent to 1-D boundary condition for the potential field. This equivalent 1-D boundary condition for the electrical potential is not quite realistic for practical PEM fuel cells because the bipolar plates with flow channels facing the electrode surfaces will make the potential boundary condition two- or three-dimensional, depending on the flow channel configurations. However, even for the present 1-D potential boundary condition, as shown in Figure 5, the potential difference between the solid and the membrane phase in the catalyst layers, which is needed to drive up the rate of the electrochemical reaction, is clearly two-dimensional. As Equation 6 indicates, the rate of reaction depends

exponentially on the potential difference between the solid and membrane phase, one-dimensional approximation could lead to significant deviations for the present simplified PEM fuel cell configuration. It might also be mentioned that the potential difference in the cathode catalyst layer is much larger than the corresponding value in the anode catalyst layer, similar to the one-dimensional results shown in Figure 2.

The two-dimensionality for the present case arises from the two-dimensional distribution of the reactant concentrations in the electrode and catalyst layers due to the variation of the reactant concentration along the flow direction in the flow channels, as pointed out

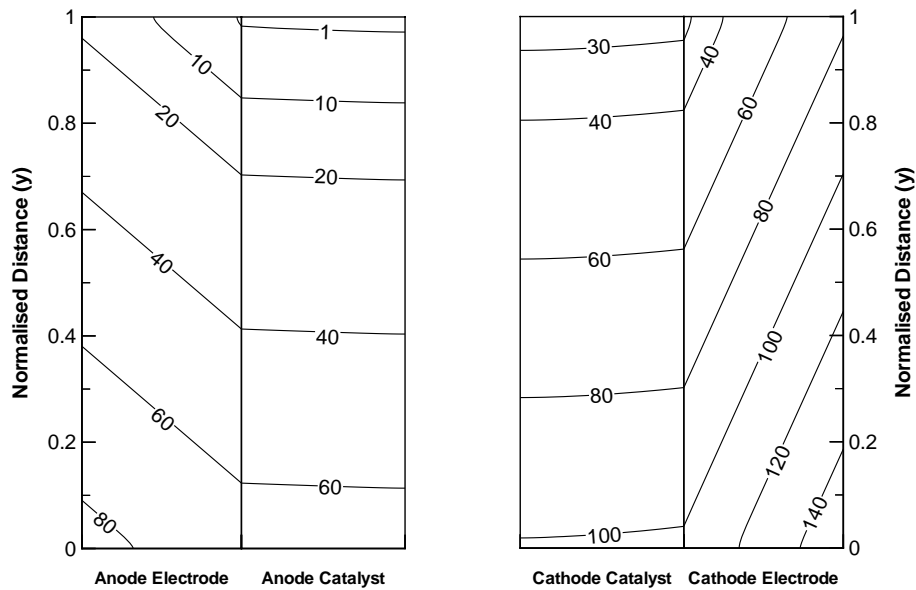


Fig. 6. Distribution of reactant concentration (mol m^{-3}) across the cell for $\eta_{\text{cell}} = 0.26$ V and co-flow of reactant streams. Anode values are for hydrogen and cathode values are for oxygen. The catalyst layer thickness has been magnified significantly for the clarity of presentation.

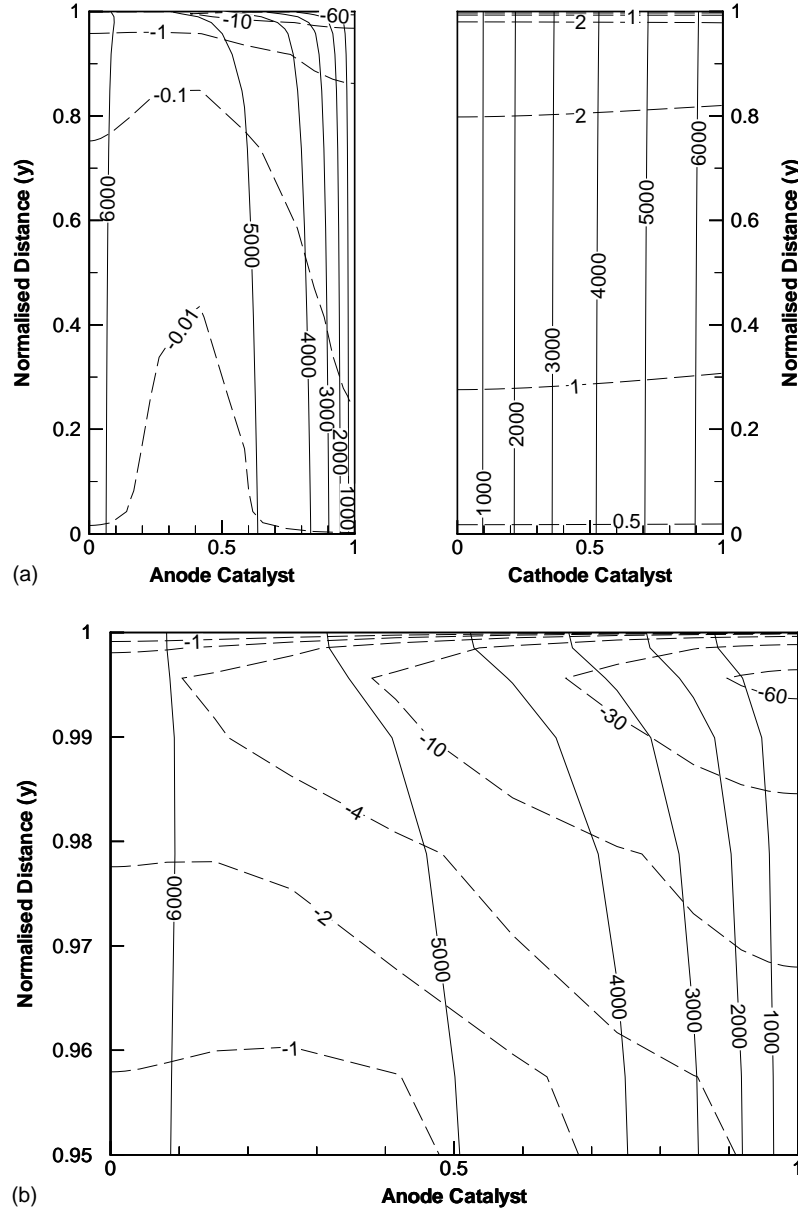


Fig. 7. Distribution of electronic current density ($A\ m^{-2}$) in the catalyst layers (a) for $\eta_{cell} = 0.26\ V$ and co-flow of reactant streams. Solid and dashed lines denote current density in the x - and y -direction, respectively. (b) A close-up of the anode catalyst layer.

earlier. The concentration distribution is shown in Figure 6, obtained under the same condition as for Figure 5. It is seen in Figure 6 that the slope for oxygen is steeper than that for hydrogen, reflecting the fact that hydrogen diffusion coefficient, hence the rate of mass transfer, is larger than the counterpart for oxygen. Also because the fuel stream pressure is only 3 bar, lower than 5 bar used for the oxidant stream, the hydrogen concentration is also lower than the oxygen in the electrode and catalyst layer at the small cell overpotential $\eta_{cell} = 0.26\ V$. It is expected that as η_{cell} is increased further, oxygen concentration in the catalyst layer will be lowered faster than hydrogen due to the smaller rate of mass transfer for oxygen molecules.

The corresponding current density distribution is shown in Figure 7a for the electronic current density

in both x and y directions, and a close-up for the anode catalyst layer in Figure 7b. A quick examination reveals the two-dimensionality of the current density distribution, especially for the y -component of the electronic current density. The local area of the low hydrogen concentration near the top right corner decreases the catalytic reaction, demanding higher values of the solid potential to accelerate the reaction process. Such a localized area of high solid potential produces a y -component current, as clearly shown in Figure 7b. The decreased reaction rate is reflected by the relatively low solid current density in the x direction near the low concentration area. It is also evident that the y -component current density is much smaller than the x -component, which contributes to the total cell current density output, hence the cell power output. It is

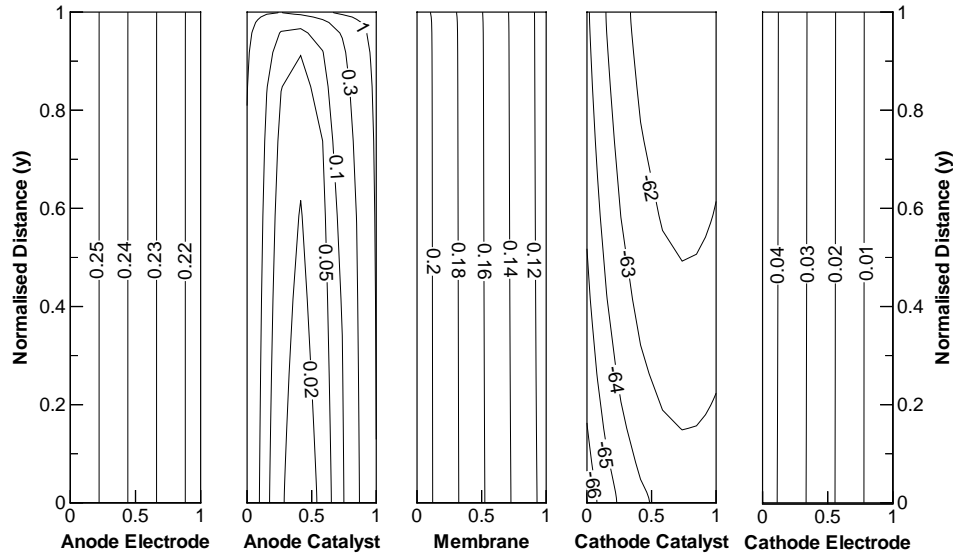


Fig. 8. Electrical potential distribution across the cell for $\eta_{\text{cell}} = 0.26$ V and counter-flow of reactant streams. Solid potential, V_s (V), in the electrode-backing layer; V_m (V), in the membrane electrolyte region; and the potential difference, $V_s - V_m$ (mV), in the catalyst layer. The catalyst layer thickness has been magnified significantly for the clarity of presentation.

expected that as the cell overpotential is increased, the y -component current density will increase significantly, hence the overpotential in the catalyst layers.

Similar calculations have been conducted when the fuel and oxidant streams are arranged in counter flow situation, i.e., in the opposite directions. This is achieved by having the fuel stream flow upwards and the oxidant stream downwards. Very similar results are obtained for the distribution of the potential, reactant concentration, reaction rate and current density as shown earlier for the co-flow case. The only discernible difference is the distribution curve in the cathode that aligns with the direction of the oxidant flow, and this is illustrated in Figure 8 for the potential distribution across the cell. The similarity is evident when compared to the results of co-flow case shown in Figure 5. Therefore, other results may be easily obtained from the co-flow results presented earlier. However, at higher cell overpotential η_{cell} this mirroring effect with only subtle difference is expected to break down between the co-flow and counter-flow cases.

The effect of utilization on the attainable power density, P'' (W m^{-2}), is investigated for both co- and counter-flow situations. The variation of the reactant concentration in the flow channel is assumed to be linear from the channel inlet to the outlet, and P'' is computed according to

$$P'' = V_{\text{cell}} \times J_{\text{cell}}$$

where the average cell current density J_{cell} (A m^{-2}) is equal to the area-averaged x -component of the current density. The utilization is varied with 0, 40 and 80% for hydrogen and 0, 25 and 50% for oxygen, as summarized in Table 2. Notice that the flow direction becomes irrelevant when the utilization is zero for at least one of the reactants. For easy comparison, the maximum attainable power density for each case has been determined and they are shown in Figure 9, where the utilization case number is defined in Table 2.

Table 2. Combinations of utilizations and flow directions used for the determination of maximum power density

Case No.	Flow Direction	H ₂ Utilization	O ₂ Utilization
1	Counter-flow	80%	50%
2	Co-flow	80%	50%
3	Counter-flow	80%	25%
4	Co-flow	80%	25%
5	N/A	80%	0%
6	Counter-flow	40%	50%
7	Co-flow	40%	50%
8	N/A	0%	50%
9	Counter-flow	40%	25%
10	Co-flow	40%	25%
11	N/A	0%	25%
12	N/A	40%	0%
13	N/A	0%	0%

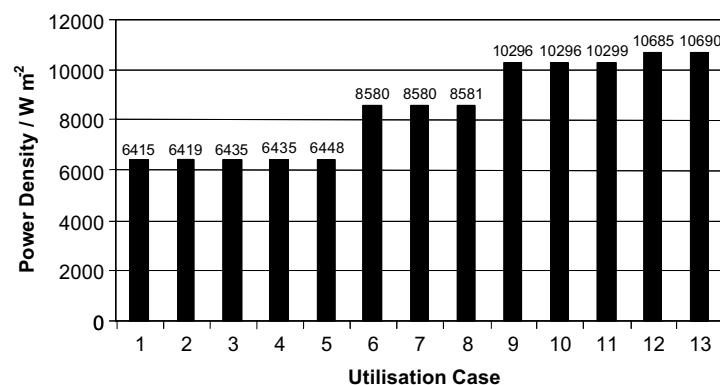


Fig. 9. Maximum power densities for various utilization cases defined in Table 2.

From Figure 9, it seems apparent that for all the cases studied the maximum power density P''_{\max} can be classified into four groups (i.e., $P''_{\max} = 6400$, 8600, 10,300 and 10,700 W m⁻²). Further investigation indicates that each group is formed by cases with the same limiting reactant. For example, for the group of $P''_{\max} = 6400$ W m⁻², the limiting reactant is hydrogen, which becomes depleted first in the catalyst layer as compared to the oxygen. In the rest of groups, the limiting reactant is seen to be oxygen, which vanishes first in the catalyst layer; while the variations of hydrogen utilization and the direction of flow have little effect on the maximum power density P''_{\max} . This may be counter intuitive since it is known, for example, that counter-flow heat exchangers are more effective for heat transfer than co-flow heat exchangers. Figure 9 also suggests that the maximum power density is increased when the oxygen utilization is lowered. Therefore, the fuel and oxidant supply should be matched in order to provide optimal performance.

5. Conclusions

Two-dimensional numerical simulations have been conducted for a steady, isothermal, fully humidified PEM fuel cell, with particular attention to the transport phenomena and electrochemical reactions occurring in the catalyst layers. Finite volume method is used along with the alternating direction implicit algorithm. The results show that the cathode catalyst layer exhibits more pronounced changes in potential, reaction rate and current density generation than the anode catalyst layer counterparts, due to the large cathode activation overpotential and the relatively low diffusion coefficient of oxygen. It is shown that the catalyst layers are two-dimensional in nature, particularly in areas of low reactant concentrations. Investigation of the combinations for the reactant utilization and flow direction suggests that maximum power density attainable is limited by the depletion of one of the reactants in the catalyst layer, simultaneous management of both fuel and oxidant supply is required for optimal cell perfor-

mance, and flow direction has little impact on the cell performance. The present analysis can be applied to more complex cell design, such as cross flow between reactant streams, and practical serpentine flow channel design.

Acknowledgements

The financial support of the Natural Sciences and Engineering Research Council (NSERC) of Canada is greatly appreciated.

References

1. T.R. Ralph, G.A. Hards, J.E. Keating, S.A. Campbell, D.P. Wilkinson, M. Davis, J. St-Pierre and M.C. Johnson, *J. Electrochem. Soc.* **144** (1997) 3845.
2. S. Gamburzev, C. Boyer and A.J. Appleby, Proc. of 1998 Fuel Cell Seminar (1998) pp. 556–559.
3. Y.W. Rho, O.A. Velev, S. Srinivasan and Y.T. Kho, *J. Electrochem. Soc.* **141** (1994) 2084.
4. J. Kim, S.M. Lee, S. Srinivasan and C.E. Chamberlin, *J. Electrochem. Soc.* **142** (1995) 2670.
5. D. Chu, R. Jiang and C. Walker, *J. Appl. Electrochem.* **30** (2000) 365.
6. R.F. Mann, J.C. Amphlett, M.W. Fowler, M.A.I. Hooper, B.A. Peppley and C.P. Thurgood, 'A generalized steady-state electrochemical model for a PEM fuel cell', Proceedings of the 9th Annual Conference of the CFD Society of Canada (University of Waterloo, Waterloo, Ontario, Canada, May 27–29 2001) pp. 376–381.
7. S. Dutta, S. Shimpalee and J.W. Van Zee, *J. Appl. Electrochem.* **30** (2000) 135.
8. H. Liu, T. Zhou and L. You, 'Modeling of proton exchange membrane fuel cells using CFD', Proceedings of the 9th Annual Conference of the CFD Society of Canada (University of Waterloo, Waterloo, Ontario, Canada, May 27–29 2001) pp. 356–362.
9. D. Singh, D.M. Lu and N. Djilali, *Int. J. Eng. Sci.* **37** (1999) 431.
10. P. Futerko and I-M. Hsing, *Electrochim. Acta* **45** (2000) 1741.
11. D. Natarajan and T.V. Nguyen, *J. Electrochem. Soc.* **148** (2001) A1324.
12. C. Marr and X. Li, *ARI* **50** (1998) 190.
13. C. Marr and X. Li, *J. Power Sources* **77** (1999) 17.
14. J.J. Baschuk and X. Li, *J. Power Sources* **86** (2000) 181.
15. A. Rowe and X. Li, *J. Power Sources* **102** (2001) 82.
16. J.J. Baschuk and X. Li, *Int. J. Energy Res.* **25** (2001) 695.

17. J.J. Baschuk and X. Li (2001) Seventh Grove Fuel Cell Symposium (London, UK, Sept. 11–13).
18. A.A. Kulikovskiy, J. Divisek and A.A. Kornyshev, *J. Electrochem. Soc.* **147** (2000) 953.
19. Ch. Wieser, A. Helmbold and E. Gulzow, *J. Appl. Electrochem.* **30** (2000) 803.
20. K.A. Hoffmann and S.T. Chiang, 'Computational Fluid Dynamics', Vol. 1 (Eng. Education System, 3rd edn, 1998).
21. B. Hum, 'Simulation of polymer electrolyte membrane fuel cells', M.A.Sc. thesis (University of Waterloo, Waterloo, Ontario, Canada, 2001).